Modulating the External Facets of Functional Nanocrystals Enabled by Two-Dimensional Oxide Crystal Templates

Huiyu Yuan,[*,†] Kai Han, David Dubbink, Guido Mul, and Johan E. ten Elshof[*]

MESA+ Institute for Nanotechnology, University of Twente, P.O. Box 217, Enschede, 7500 AE, The Netherlands

S *Supporting Information*

ABSTRACT: The nature of the external crystal facets is critical to control the (photo)catalytic properties. Two-dimensional materials can expose only one type of crystal facet among zero-dimensional (0D), one-dimensional (1D), and two-dimensional (2D) materials. Controllable tuning of the nature of the external crystal facets of 2D materials is highly desirable but very challenging. Here, we show that 2D particles with the desirable crystal facet for high-performance photocatalytic H_2 generation can be obtained by using 2D metal oxide materials (i.e., nanosheets of $Ca_2Nb_3O_{10}$ and $Ti_{0.87}O_2$) as templates taking consideration of the crystal configuration of 2D oxide and target compounds. We demonstrate that anatase TiO_2 crystals grown on different nanosheet templates exhibit variations in photocatalytic hydrogen production rates from aqueous phase methanol solutions (6.7%), which can be attributed to the nature of the main crystal facet exposed. In view of the large number of 2D materials that have already been synthesized, this work offers a key to design and synthesize nanoparticles with the desirable specific external crystal facet for (photo)catalysis application.

KEYWORDS: *2D oxides, nanosheet, template synthesis, preferential crystal facet, photocatalytic hydrogen evolution*
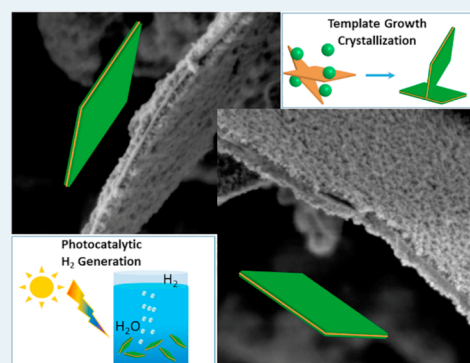
Engineering the crystal orientation is essential for many applications, especially for (photo)catalysts and lithium ion batteries (LIBs).[1,2] For example, the photoactivity of anatase TiO_2 crystals is dependent on the nature of the exposed crystal facets, where the reactivity decreases in the order {010} > {101} > {001}.[1] In LIBs, $LiFePO_4$ nanoplatelets with crystal orientation along the *ac* and *bc* facets present quite different reversible gravimetric capacities at high C-rates.[3] The *ac* oriented crystals deliver 148 mAh g^{-1} at 10 C-rate, while the *bc* faceted crystals deliver only 28 mAh g^{-1}.[3] So, facile methodologies to synthesize crystallites with controlled orientation and single facet are highly desirable. Two-dimensional (2D) materials have been emerging as a promising class of nanomaterials for various applications, including LIBs,[4] supercapacitors,[5] photovoltaics,[6] catalysis[7] and electronics.[8] Their 2D nature endows those materials the unique possibility to expose only a single type of crystal facet, in contrast to most other low-dimensional materials such as (0D) nanoparticles and (1D) nanowires. So controllable synthesis of 2D materials with desirable crystal facets is a very promising approach to achieve high material performance. However, the challenge is that the state-of-the-art synthesis methods for crystals in thin film morphologies often lack control over crystal orientation. To date, the exfoliation method is the most used synthesis method for 2D nanosheets. The crystal orientation of 2D nanosheets produced by this method is dictated by their bulk counterparts.[9,10] Even though several new approaches have been reported to synthesize 2D nanosheets,[11,12] controlled

manipulation of 2D nanosheets' crystal orientation has not been reported.

Recently, it has been shown that metal oxide nanosheet films are able to serve as a seed layer for epitaxial growth of functional oxide thin films by solution and vapor-phase deposition methods.[13−15] The crystal orientation of thin films on nanosheets could be controlled by the nature, more specifically, the 2D lattice parameters of the nanosheets.[13,15,16] The success of employing oxide nanosheets as seed layers for thin film growth also offers a strategy for the development of nanoparticles with preferred crystal orientation. Additional advantages of using 2D oxides as templates are their tunable lateral sizes,[8,17−19] diversity in composition,[9,20,21] and facile synthesis,[22−25] which offers ample opportunities to design and control the final material. Templated synthesis has been demonstrated as a powerful tool to direct the formation of nanomaterials into forms that are otherwise difficult to obtain, such as nanospheres, nanotubes, and nanowires.[26−28] Sb_2Te_3 nanoplatelets have been reported as templates to synthesize 3D porous nanothread-based (or nanotube-based) metal and metal telluride nanoplates.[29] Recently, Wu et al. reported successful synthesis of nanoarray/nanosheet 3D structure by using 2D CuS/CdS nanosheets via wet chemical synthesis.[30] However, most materials need some thermal after-treatment to obtain well-crystallized material. Hence, a nanosheet seeding techni-

que can lead to successful formation of crystallographically engineered 2D-like nanoparticles provided that the nanosheets can survive the conditions during the wet-chemical synthesis and thermal annealing process steps. Interestingly, 2D oxides have been demonstrated to have much better thermal stability than their bulk counterparts. The monolayer titanate nanosheets undergo phase transformation at 800 °C compared to the bulk at 400−500 °C.[31] This has motivated us to explore the controllable manipulation of 2D nanosheets' crystal orientation by using nanosheets as templates.

In this article, we demonstrate, for the first time, that 2D oxide nanosheets can guide the crystallographic growth direction and yield 2D-like oxide platelets with preferential crystal orientation by employing a wet-chemical synthesis route followed by calcination (see schematic in Figure 1a). The
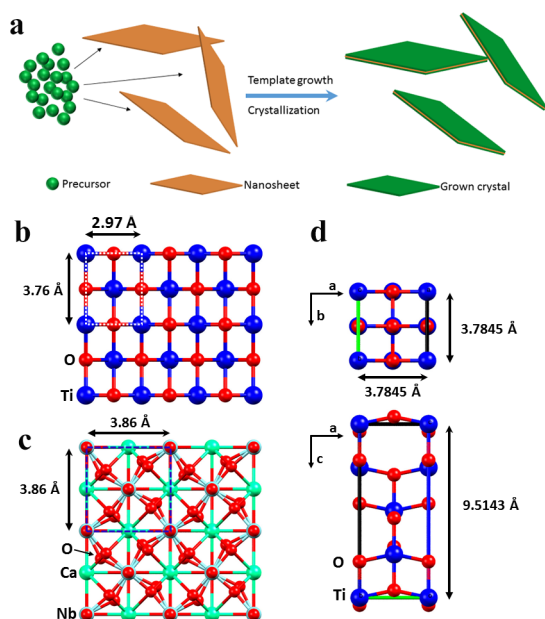

Figure 1. (a) Schematic representation of synthesis strategy. The in-plane crystal configuration of (b) TO and (c) CNO nanosheets. (d) The crystal structure of TiO_2 anatase phase.

results prove the principle that nanosheets can be used as templates for the synthesis of 2D particles with preferential orientation, and that this approach has the obvious advantages of a free and rich choice of template, ease of synthesis and control over composition and crystal structure. Two types of 2D oxide nanosheet seed crystals, namely titanate ($Ti_{0.87}O_2$, further denoted as TO; thickness 0.75 nm) and calcium niobate ($Ca_2Nb_3O_{10}$, denoted as CNO; thickness 1.44 nm) nanosheets were synthesized by chemical exfoliation of their layered bulk counterparts as described elsewhere.[8,22] Figure 1b,c show the in-plane crystal configuration of TO and CNO nanosheets, respectively. The TO nanosheets have a rectangle configuration with $a = 2.97$ Å and $b = 3.76$ Å, while the CNO nanosheets have a square configuration with $a = b = 3.86$ Å.[13] We chose the catalytically active anatase phase of titanium dioxide as a model material. The anatase is in the tetragonal system, and the lattice parameters of anatase are $a = b = 3.7845$ Å, $c = 9.5143$ Å (see Figure 1d). The largest lattice mismatch between anatase and TO nanosheets for a or b axis oriented growth is +6.78%, which is much smaller than the mismatch of +27.42% between c axis-oriented anatase and TO nanosheets. Hence, c axis oriented

growth of anatase on TO nanosheets is energetically unfavorable. For CNO nanosheets, the lattice mismatch for c axis oriented growth of anatase is only −1.96%. Therefore, TO and CNO nanosheets were therefore expected to promote growth of the anatase phase along the a or b axis and c axis, respectively.

Anatase crystallites were grown on the TO and CNO nanosheet seed layers via a facile synthesis route.[32−34] The synthesized NanoSheet Templated Crystals (NSTC), denoted as TO-NSTC and CNO-NSTC crystals, respectively, were compared with anatase crystallites formed under similar conditions but in the absence of nanosheets (denoted here as NO crystals). The morphology and crystal structure of the TO-NSTC, CNO-NSTC, NO crystals, and the nanosheets were characterized by high-resolution scanning electron microscopy (HRSEM), powder X-ray diffraction (PXRD), and atomic force microscopy (AFM). Further experimental details can be found in the Methods section. The HRSEM images in Figure 2a−e show that the shape of the TO-NSTC and CNO-NSTC crystals is platelet-like and their thickness is ∼100 nm, while the NO crystals do not show any 2D-like morphology or surface features. Figure 2a−d show that the size of the crystallites templated by nanosheets was consistent with the sizes of the nanosheet templates (see the height profiles of TO and CNO nanosheets in Figure S1). High-magnification SEM figures (Figure 2b,d) reveal that the surfaces of both the TO-NSTC and CNO-NSTC crystals are covered with small crystallites. It is noted that peeling off of the as-grown NSTC crystallites from CNO-NSTC crystals was observed (see smooth surfaces in Figure 2d), indicating weak bonding between the two interfaces. We speculate that this behavior is due to weak bonding forces between the multilayer nanosheets functioning as growth templates. The PXRD data in Figure 2f show that all three products consist of the anatase phase. In the CNO-NSTC crystals, a small peak at 2θ 23.1° is present, which is attributed to the (100) reflection of CNO nanosheets.[8] This indicates that the CNO nanosheets survive in the synthesis conditions of the CNO-NSTC crystals. No other phases appear as impurities.

High-resolution transmission electron microscopy (HRTEM) was used to investigate the anatase phase on nanosheets in more detail. Figure 3 shows that the anatase crystals on TO-NSTC and CNO-NSTC nanosheets are polycrystalline with a crystal size of ∼10 nm. Although the crystal orientation cannot be observed directly, it is possible to determine the orientation by observing the crystal planes in the direction normal to the surface. Selected area electron diffraction (SAED) patterns suggest that the TO-NSTC crystals mainly expose {100} and {001} crystal facets. The inset in Figure 3a shows Fast Fourier transform (FFT) data of a typical pattern of the crystal plane normal to the observation direction. The observed crystal planes are listed in the inset image. The presence of (002), (200), (103), (101), and (204) in the FFT patterns is due to the exposure of the {100} facet; the presence of (101), (011), (112), and (211) suggests exposure of the {001} facet (see Figure S2a). The reason for the presence of a small fraction of c-axis oriented crystalline material on TO nanosheets is probably due to reaction between TO nanosheets and anatase during the thermal annealing process. The presence of rutile phase in the TO-NSTC-derived films as a possible reaction product of this interaction supports this hypothesis (discussed next). On the other hand, the CNO-NSTC crystals expose the {001} facet as their majority facet, which gives rise to the crystal planes of (101), (011), (112), and (211) (see
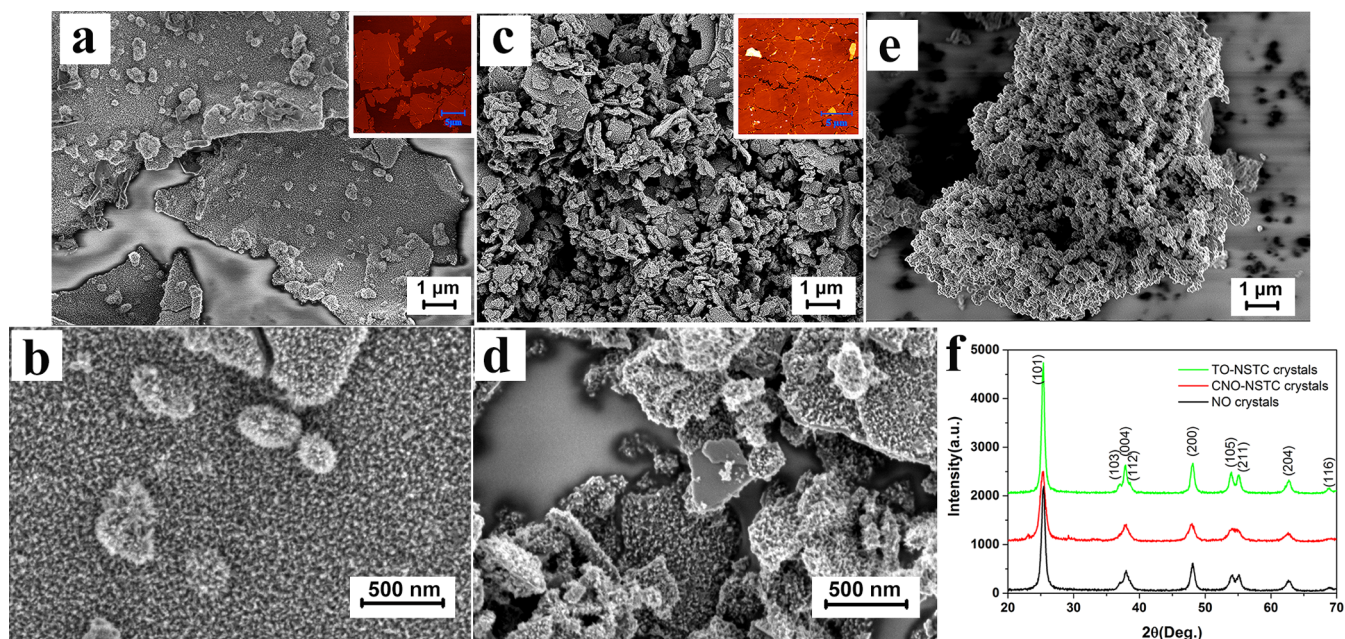
Figure 2. HRSEM images of (a,b) TO-NSTC, (c,d) CNO-NSTC, and (e) NO crystals. The insets in panels a and c show AFM images of as-deposited nanosheets by Langmuir−Blodgett (LB) deposition; (f) PXRD patterns of templated and nontemplated anatase crystallites.
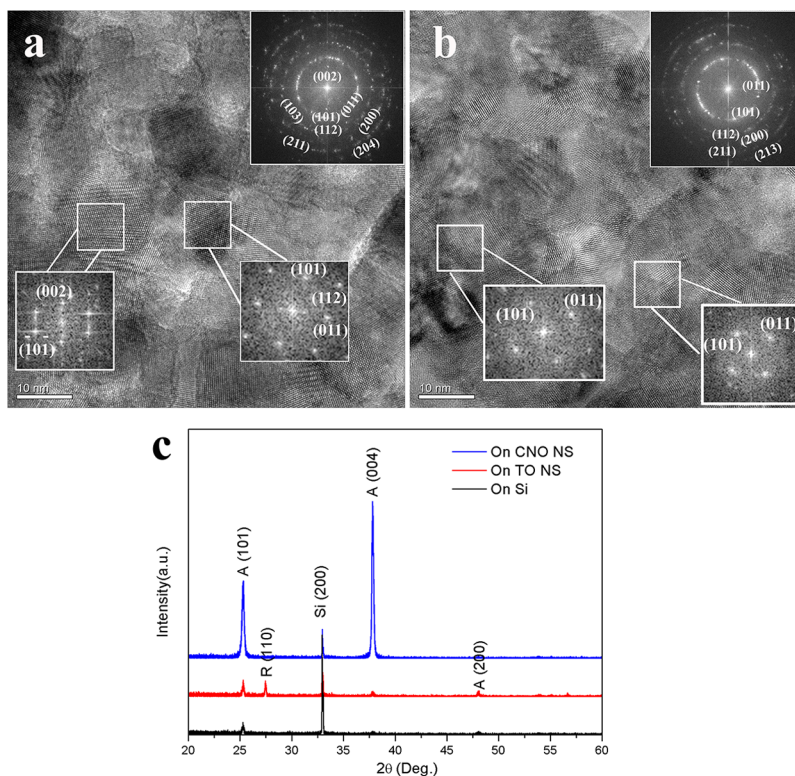

Figure 3. HRTEM images of (a) TO-NSTC and (b) CNO-NSTC crystals. Insets in the upper right corners show fast Fourier transform (FFT) patterns of the whole TEM images. The other insets present the typical FFT patterns in selected areas of the samples. (c) PXRD of TiO$_2$ thin films grown on Si, TO, and CNO nanosheets.

Figure S2b,c). All crystal planes visible in the inset of Figure 3b, i.e. (101), (011), (112), (200), (211), and (213), are in agreement with this hypothesis, even though the observation direction is not along the *c* axis but under an angle (see Figure S2b,c). The deviation between the observation direction and the *c* axis is probably related to the surface morphology of covering small crystallites.

We confirmed the preferential crystal growth direction on nanosheets by growing TiO$_2$ anatase on Langmuir−Blodgett (LB) monolayer films of nanosheets. Anatase crystals grown on LB films of TO and CNO nanosheets showed similar results as described above (Figure 3c). The TO-NSTC thin film on TO nanosheets showed both (001) and (100) peaks, while the CNO nanosheets yielded preferentially oriented growth along
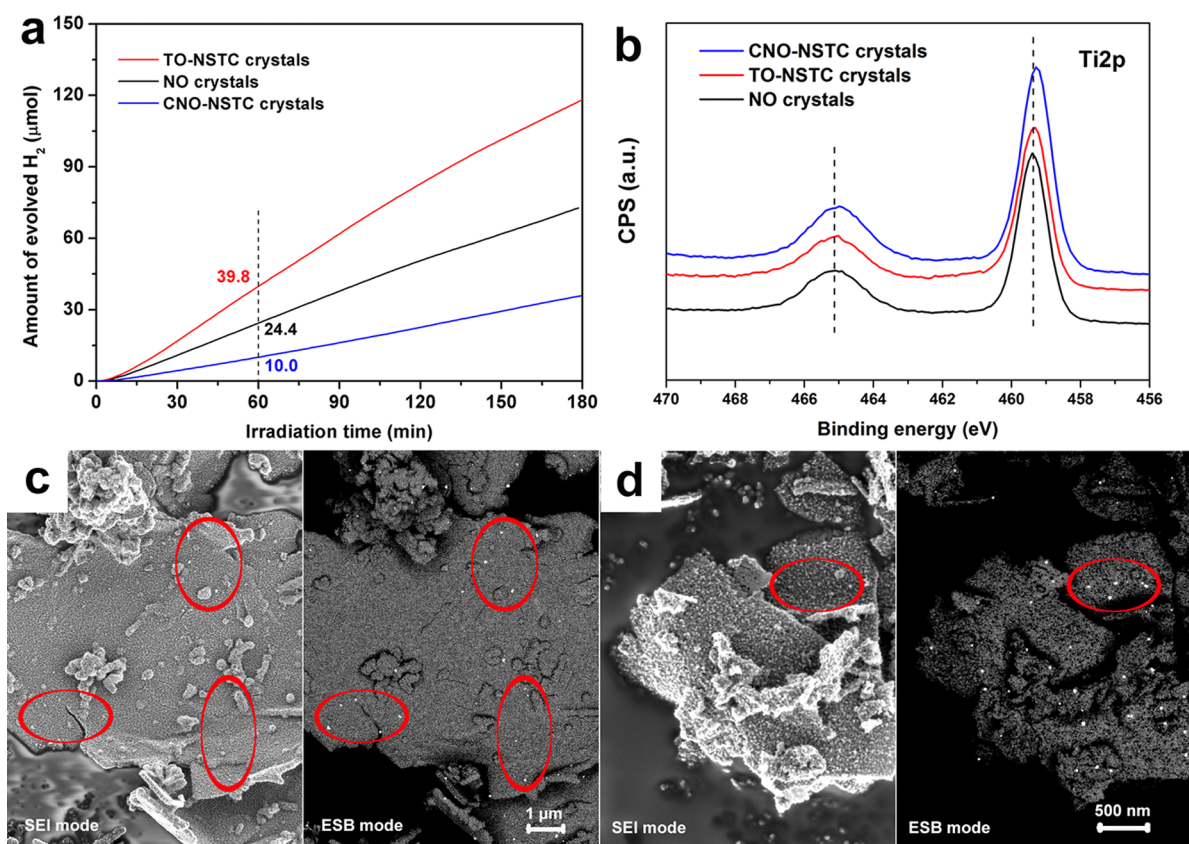
Figure 4. (a) Hydrogen evolution rate from water containing 6.7 vol % methanol using TO-NSTC, NO, or CNO-NSTC crystals. (b) Ti 2p XPS spectra of TO-NSTC, NO, and CNO-NSTC. (c,d) HRSEM images of (c) TO-NSTC and (d) CNO-NSTC. Left image: secondary electron imaging (SEI) analysis; Right: energy selective backscattered electron (ESB) analysis. Red circles indicate the location of some of the Pt nanoparticles on the surface of the platelets.

the (001) direction. The (101) peaks in both thin film samples are probably due to lack of full substrate coverage by the nanosheets, so that some nontemplated crystal growth occurs next to oriented growth. A small fraction of rutile phase was present in the anatase thin film on TO nanosheets, but not on CNO nanosheets. Most likely rutile was formed by transformation of anatase, for which a pure TiO_2 phase is required. The absence of rutile in anatase grown on CNO sheets may be related to the fact that the presence of minor concentrations of foreign elements in or next to the anatase phase usually inhibits the phase transformation of anatase into rutile effectively.[35]

The photocatalytic activity of the three types of anatase for H_2 generation from a mixture of water and methanol decreased in the order TO-NSTC > NO > CNO-NSTC, as shown in Figure 4a. The absolute values of H_2 production performance for TO-NSTC, NO, and CNO-NSTC are 39.8, 24.4, and 10.0 μmol h^{-1}, respectively. It is noted that optimization of the experimental conditions such as the amount of catalyst and Pt is expected to improve these values. However, the optimization work, falling beyond the scope of this work for demonstration of rational synthesis of 2D nanoparticles with controlled external crystal facets, will be shown elsewhere. We first confirmed the absence of N and F as impurities in all the samples (see Figure S3a−c). We further confirmed by X-ray fluorescence (XRF) that the Pt concentration in all three samples was ~1%. The XPS analysis of Pt particles shows that the Pt in all three samples has a comparable oxidation state (see Figure S 3d). The chemical state of Ti in the three types of crystals was slightly different (Figure 4b). The Ti 2p peaks of

CNO-NSTC crystals were shifted to slightly lower binding energy (−0.1 eV), indicating a small degree of electron gain (reduction) of Ti atoms from surrounding atoms,[36] probably niobium introduced via the nanosheet templates (see Figure S3b). Furthermore, the specific surface area of CNO-NSTC, 83 m^2/g, is much larger than that of TO-NSTC and NO crystals (i.e., 57 and 57 m^2/g, respectively; see the BET curves in Figure S4). This result is in good agreement with the observation that the CNO-NSTC crystals are smaller than the TO-NSTC crystals (see Figure 2a−e). The distribution of Pt on the TO-NSTC and CNO-NSTC crystals is shown in Figure 4c,d. Pt particles on TO-NSTC and CNO-NSTC were mainly found at the edges of the platelets, especially for CNO-NSTC. Only few Pt particles were seen on the surface of TO-NSTC crystals (indicated by red circles in Figure 4c). There are even fewer Pt particles on the surface of CNO-NSTC crystals. Compared to the TO-NSTC and CNO-NSTC crystals, the NO crystals showed a uniform Pt distribution (see more data in Figure S5).

The distribution of Pt on the crystal surfaces provides an indication of the distribution of photoactive sites. The higher the photoactivity of the surface location is, the more favorable it is for Pt deposition. It is known that the photoactivity of TiO_2 anatase facets decreases in the order {010} > {101} > {001}.[1] Hence, Pt particles are expected to form most easily on {010} facets. The distribution of Pt on TO-NSTC and CNO-NSTC crystals is consistent with the crystallographic data that confirmed that TO-NSTC crystals expose a mixture of {010} and {001} facets, while CNO-NSTC crystals expose almost exclusively {001} facets. We believe that the higher photo-

catalytic hydrogen evolution activity of the TO-NSTC crystals is due to the presence of {010} facets, while the exposure of {001} facets is responsible for the low photocatalytic performance of CNO-NSTC crystals. And because of the absence of templates, NO crystals expose a mixture of facets, including some {010}. So, the photocatalytic activity of NO crystals is higher than that of CNO-NSTC crystals, even though some reduction of Ti in CNO-NSTC crystals was observed.[37] It is noted that by tuning of the portions of exposed facets, it may be possible to enhance the photocatalytic activity.[38,39] For example, the coexistence of {010} and {001} facets could lead to higher activity. Further work to control these fractions in these 2D systems is needed to verify this hypothesis. The photocatalytic activity of TO-NSTC in this work is found to be higher than the anatase in different morphologies but lower than the nanosheet-anatase with smaller thickness or doped anatase (see Table S1), indicating the superiority of this strategy.

In summary, we have demonstrated a facile method to synthesize 2D TiO_2 anatase with preferential growth orientation by using metal oxide nanosheets as a template for nucleation and guided growth. The photocatalytic activity of anatase can be controlled by the choice of template, which will lead to the exposure of specific crystallographic facets. Considering the large number of members in the 2D materials family,[10] we believe that by proper experimental design this method is also applicable to guide crystallographic growth direction and thickness of other oxide and nonoxide compounds, offering rich scenarios for synthesis of crystals with a single-crystal facet.

■ METHODS

Preparation of TO-NSTC, CNO-NSTC, and NO Crystals. The layered phases $K_{0.8}Ti_{1.73}Li_{0.27}O_4$ (KLTO) and $KCa_2Nb_3O_{10}$ (KCNO) were prepared by high temperature sintering of Li_2CO_3, K_2CO_3, and TiO_2 for KLTO, and K_2CO_3, $CaCO_3$, and Nb_2O_5 for KCNO. The as-obtained particles were protonated into their solid acid forms $H_{1.07}Ti_{1.73}O_4$ (HTO) and $HCa_2Nb_3O_{10}$ (HCNO). Chemical exfoliation was done in aqueous solution by reacting the protonated oxides with tetra-butylammonium hydroxide (TBAOH). The molar ratio of TBA^+/H^+ (where H^+ refers to the equivalent number of protons in the protonated oxides) was 4/1 for HTO and 2/1 for HCNO nanosheets.[8,22,40] The nominal nanosheet concentration in solution was 5 g/L for both types of nanosheets. For the synthesis of anatase, $(NH_4)_2TiF_6$ and H_3BO_3 were used as precursors. The molar ratio of $(NH_4)_2TiF_6/H_3BO_3$ was 1/2, and the $(NH_4)_2TiF_6$ concentration was 0.1 mol/L. After mixing $(NH_4)_2TiF_6$ and H_3BO_3 for 5 min in aqueous solution, 45.7 μmol of TO or CNO nanosheets were added. Anatase TiO_2 without nanosheets was also prepared for the sake of comparison. After 2 days of crystal growth, the resulting particles were washed and collected by filtration. The resulting powders were annealed at 450 °C in air. The final powders made using TO and CNO nanosheets are denoted as TO-NSTC and CNO-NSTC crystals, respectively. The powders prepared without nanosheet are denoted as NO crystals.

Photodeposition of Pt on TiO_2 Anatase Crystals and Hydrogen Generation Test. For Pt deposition, 0.1 g of each sample was added to a solution containing 30 mL of water and 5 mL of 420 mg/L chloroplatinic acid (H_2PtCl_6). Subsequently, 3 mL of methanol was added, and the system was illuminated under 3.21 mW cm^{-2} at 375 nm for 5 h. Then, the mixture was centrifuged (8500 rpm, 10 min) and washed with water three more times. The powders were dried overnight at 75 °C, so that 1 wt % platinum loaded samples were obtained.

Hydrogen Detection. The hydrogen formation rate of all powders was tested by adding 15 mg of powder to a solution containing water and 6.7 vol % methanol, with a total volume of 15 mL. The reactor was connected to a gas chromatograph (GC), equipped with a Parabond Q column (10 m) and a TCD detector to determine the H_2 and O_2 concentrations. The solution was purged for ∼1 h in the dark before illumination. Illumination came from an optical fiber connected to a 120 W high pressure mercury lamp from Dr. Gröbel UC-Elektronik GmbH, with a spectral range from 280 to 650 nm.

Characterization. High-resolution scanning electron microscopy (HRSEM; Zeiss MERLIN) was used to acquire information on the morphology, particle thickness, and Pt distribution. Powder X-ray diffraction (PXRD) data were acquired on a Bruker D2 PHASER (Cu Kα radiation with a wavelength of 0.15405 nm). X-ray diffraction patterns of all the thin film samples were acquired by on a Philips X'Pert X-ray Diffractometer (Cu Kα radiation with a wavelength of 0.15405 nm). Transmission electron microscopy (TEM) was performed on a Philips CM300ST-FEG at 300 kV, with the sample supported on a carbon microgrid. X-ray photoelectron spectroscopy (XPS) measurements were conducted on an Omicron nanotechnology GmbH (Oxford Instruments) Surface Analysis system with a photon energy of 1486.7 eV (Al Kα X-ray source) with a scanning step size of 0.1 eV. The pass energy was set to 20 eV. The spectra were corrected using the binding energy of C 1s of the carbon tape as a reference. X-ray fluorescence spectroscopy (XRF; Philips PW 1480, including FPMulti-software from Panalytical B. V.) was employed to analyze the elemental composition.

■ ASSOCIATED CONTENT

Ⓢ Supporting Information

The Supporting Information is available free of charge on the ACS Publications website at DOI: 10.1021/acscatal.7b02605.

> Experimental details for LB deposition and liquid phase deposition; AFM images and height profiles of CNO and TO nanosheets; schematic of crystal orientation observed; XPS survey spectra and XPS spectra of Pt 4f at TO-NSTC, NO, and CNO-NSTC crystals; BET isotherm curves of the CNO-NSTC, TO-NSTC, and NO crystals; energy-selective backscattered (ESB) HRSEM images of TO-NSTC, CNO-NSTC, and NO crystals; table of data set of H_2 production rate from literature (PDF)

■ AUTHOR INFORMATION

Corresponding Authors
*E-mail: yuanhuiyu01@gmail.com.
*E-mail: j.e.tenelshof@utwente.nl.

ORCID Ⓞ
Huiyu Yuan: 0000-0002-5302-3519
Johan E. ten Elshof: 0000-0001-7995-6571

Present Address
†H.Y.: Department of Applied Physics, The Hong Kong Polytechnic University, Hung Hom, Kowloon, Hong Kong.

Notes
The authors declare no competing financial interest.

■ REFERENCES

(1) Pan, J.; Liu, G.; Lu, G. Q.; Cheng, H.-M. *Angew. Chem., Int. Ed.* **2011**, *50*, 2133−2137.

(2) Ganapathy, S.; Wagemaker, M. *ACS Nano* **2012**, *6*, 8702−8712.

(3) Wang, L.; He, X.; Sun, W.; Wang, J.; Li, Y.; Fan, S. *Nano Lett.* **2012**, *12*, 5632−5636.

(4) Compton, O. C.; Abouimrane, A.; An, Z.; Palmeri, M. J.; Brinson, L. C.; Amine, K.; Nguyen, S. T. *Small* **2012**, *8*, 1110−1116.

(5) Peng, X.; Peng, L.; Wu, C.; Xie, Y. *Chem. Soc. Rev.* **2014**, *43*, 3303−3323.

(6) Bai, Y.; Xing, Z.; Yu, H.; Li, Z.; Amal, R.; Wang, L. *ACS Appl. Mater. Interfaces* **2013**, *5*, 12058−12065.

(7) Yui, T.; Tsuchino, T.; Itoh, T.; Ogawa, M.; Fukushima, Y.; Takagi, K. *Langmuir* **2005**, *21*, 2644−2646.

(8) Yuan, H.; Nguyen, M.; Hammer, T.; Koster, G.; Rijnders, G.; ten Elshof, J. E. *ACS Appl. Mater. Interfaces* **2015**, *7*, 27473−27478.

(9) Ma, R.; Sasaki, T. *Acc. Chem. Res.* **2015**, *48*, 136−143.

(10) Nicolosi, V.; Chhowalla, M.; Kanatzidis, M. G.; Strano, M. S.; Coleman, J. N. *Science* **2013**, *340*, 1226419.

(11) AbdelHamid, A. A.; Yu, Y.; Yang, J.; Ying, J. Y. *Adv. Mater.* **2017**, *29*, 1701427.

(12) Xiao, X.; Song, H.; Lin, S.; Zhou, Y.; Zhan, X.; Hu, Z.; Zhang, Q.; Sun, J.; Yang, B.; Li, T.; Jiao, L.; Zhou, J.; Tang, J.; Gogotsi, Y. *Nat. Commun.* **2016**, *7*, 11296.

(13) Nijland, M.; Kumar, S.; Lubbers, R.; Blank, D. H. A.; Rijnders, G.; Koster, G.; ten Elshof, J. E. *ACS Appl. Mater. Interfaces* **2014**, *6*, 2777−2785.

(14) Kikuta, K.; Noda, K.; Okumura, S.; Yamaguchi, T.; Hirano, S.-i. *J. Sol-Gel Sci. Technol.* **2007**, *42*, 381−387.

(15) Shibata, T.; Fukuda, K.; Ebina, Y.; Kogure, T.; Sasaki, T. *Adv. Mater.* **2008**, *20*, 231−235.

(16) Shibata, T.; Takano, H.; Ebina, Y.; Kim, D. S.; Ozawa, T. C.; Akatsuka, K.; Ohnishi, T.; Takada, K.; Kogure, T.; Sasaki, T. *J. Mater. Chem. C* **2014**, *2*, 441−449.

(17) Sasaki, T.; Watanabe, M. *J. Phys. Chem. B* **1997**, *101*, 10159−10161.

(18) Tanaka, T.; Ebina, Y.; Takada, K.; Kurashima, K.; Sasaki, T. *Chem. Mater.* **2003**, *15*, 3564−3568.

(19) Igarashi, S.; Sato, S.; Takashima, T.; Ogawa, M. *Ind. Eng. Chem. Res.* **2013**, *52*, 3329−3333.

(20) ten Elshof, J. E.; Yuan, H.; Gonzalez Rodriguez, P. *Adv. Energy Mater.* **2016**, *6*, 1600355.

(21) Ma, R. Z.; Liu, Z. P.; Li, L.; Iyi, N.; Sasaki, T. *J. Mater. Chem.* **2006**, *16*, 3809−3813.

(22) Yuan, H.; Dubbink, D.; Besselink, R.; ten Elshof, J. E. *Angew. Chem., Int. Ed.* **2015**, *54*, 9239−9243.

(23) Yuan, H.; Lubbers, R.; Besselink, R.; Nijland, M.; ten Elshof, J. E. *ACS Appl. Mater. Interfaces* **2014**, *6*, 8567−8574.

(24) Sasaki, T.; Watanabe, M. *J. Am. Chem. Soc.* **1998**, *120*, 4682−4689.

(25) Maluangnont, T.; Matsuba, K.; Geng, F.; Ma, R.; Yamauchi, Y.; Sasaki, T. *Chem. Mater.* **2013**, *25*, 3137−3146.

(26) Liu, Y.; Goebl, J.; Yin, Y. *Chem. Soc. Rev.* **2013**, *42*, 2610−2653.

(27) Kovtyukhova, N. I.; Mallouk, T. E.; Mayer, T. S. *Adv. Mater.* **2003**, *15*, 780−785.

(28) Mbindyo, J. K. N.; Mallouk, T. E.; Mattzela, J. B.; Kratochvilova, I.; Razavi, B.; Jackson, T. N.; Mayer, T. S. *J. Am. Chem. Soc.* **2002**, *124*, 4020−4026.

(29) Zhang, H.; Wang, H.; Xu, Y.; Zhuo, S.; Yu, Y.; Zhang, B. *Angew. Chem., Int. Ed.* **2012**, *51*, 1459−1463.

(30) Wu, X.-J.; Chen, J.; Tan, C.; Zhu, Y.; Han, Y.; Zhang, H. *Nat. Chem.* **2016**, *8*, 470−475.

(31) Fukuda, K.; Ebina, Y.; Shibata, T.; Aizawa, T.; Nakai, I.; Sasaki, T. *J. Am. Chem. Soc.* **2007**, *129*, 202−209.

(32) Zhou, L.; Smyth-Boyle, D.; O'Brien, P. *J. Am. Chem. Soc.* **2008**, *130*, 1309−1320.

(33) Liu, Y.; Zhang, Y.; Tan, H.; Wang, J. *Cryst. Growth Des.* **2011**, *11*, 2905−2912.

(34) Maki, H.; Okumura, Y.; Ikuta, H.; Mizuhata, M. *J. Phys. Chem. C* **2014**, *118*, 11964−11974.

(35) Hanaor, D. A. H.; Sorrell, C. C. *J. Mater. Sci.* **2011**, *46*, 855−874.

(36) Sun, Z.; Liao, T.; Dou, Y.; Hwang, S. M.; Park, M.-S.; Jiang, L.; Kim, J. H.; Dou, S. X. *Nat. Commun.* **2014**, *5*, 3813.

(37) Zhao, W.; Ai, Z.; Dai, J.; Zhang, M. *PLoS One* **2014**, *9*, e103671.

(38) Yu, J.; Low, J.; Xiao, W.; Zhou, P.; Jaroniec, M. *J. Am. Chem. Soc.* **2014**, *136*, 8839−8842.

(39) Roy, N.; Sohn, Y.; Pradhan, D. *ACS Nano* **2013**, *7*, 2532−2540.

(40) Yuan, H.; Timmerman, M.; van de Putte, M.; Gonzalez Rodriguez, P.; Veldhuis, S.; ten Elshof, J. E. *J. Phys. Chem. C* **2016**, *120*, 25411−25417.